

Temperature and electric field effects on the dynamic modes in a spin current auto-oscillatorLina Chen,^{1,2} Yaoyu Gu,² Kaiyuan Zhou,² Zishuang Li,² Liyuan Li,² Zhenyu Gao²,² Y. W. Du,² and R. H. Liu^{1,2,*}¹*School of Science, Nanjing University of Posts and Telecommunications, Nanjing 210023, China*²*National Laboratory of Solid State Microstructures, Jiangsu Provincial Key Laboratory for Nanotechnology, and School of Physics, Nanjing University, Nanjing 210093, China*

(Received 4 March 2021; accepted 8 April 2021; published 19 April 2021)

We systematically study spectral characteristics of emission microwave signal by a spin current nano-oscillator (SCNO) based on TaO_x/Py(3)/Pt(2) trilayers as a function of current, in-plane magnetic field angle, electrostatic gating, and temperature. The current dependence of spectral characteristics shows that such SCNO exhibits a single coherent oscillation mode at low currents, and then transfers into a multimode coexistence regime with several oscillation peaks, related to spatially separated oscillation regions, at high currents. The linewidth of these modes shows an exponential temperature dependence, indicating thermally activated mode transitions or mode hopping behavior among these spatially separated oscillation regions due to the mode coupling caused by strong thermal-magnon-mediated scattering rate at high temperatures. Additionally, electrostatic gating on oscillation frequency shows a temperature-independent behavior, but gets enhanced in the strongly nonlinear oscillation regime. The enhanced phenomenon is caused by a combination of nonlinear frequency redshift and driving current shift due to electric-field modulation of current-induced spin-orbit torques. The demonstrated electric-field and current control of three-terminal SCNO provides an efficient approach to developing electrically tunable microwave generators in radio frequency integrated circuits and spin-wave-based logic gates in magnonic devices.

DOI: [10.1103/PhysRevB.103.144426](https://doi.org/10.1103/PhysRevB.103.144426)**I. INTRODUCTION**

All-electric magnetization manipulation is particularly attractive because it facilitates the realization of nonvolatility, low-power, high-speed, and high-density spintronic devices and is also easy to integrate with modern semiconductor electronics. Various mechanisms and approaches enabling all-electric control of magnetism have been explored and verified in various materials and heterostructures [1–4]. For instance, electric field can reverse magnetization in multiferroic materials or artificial ferromagnetic-ferroelectric multiferroic heterostructures via charge modulation, exchange bias, and strain coupling based on inverse piezoelectric effect or inverse magnetostriction effect [2,5,6], or in ultrathin ferromagnetic films due to voltage modulation of the interfacial magnetic anisotropy [7–10]. In addition, electric-current also can induce magnetization reversal and auto-oscillation due to the spin torque effect in magnetic multilayer structures [11–14] and ferromagnet-heavy metal heterostructures (FH) [15–19]. In FH multilayers, it is generally considered that current-induced spin-orbit torques (SOTs) have two classes of mechanisms: one is due to spin-orbit coupling in the interior of the heavy metal layer, called bulk spin Hall effect (SHE) [20,21]; another is due to the spin-orbit coupling at the interfaces between layers, called interfacial Rashba-Edelstein effect (IREE) [22,23]. The former generates an out-of-plane spin current under the in-plane electric-current, which exerts a spin-transfer torque upon flowing into the ferromagnetic layer. The latter produces a nonequilibrium spin density at the inter-

face proportional to the in-plane current density, which exerts a torque on magnetization at the interface via the exchange interaction [24]. Similar to the interfacial magnetic anisotropy (IMA) [25], the torques arise from IREE can be effectively controlled by tuning the interfacial spin-orbit coupling utilizing gating voltage [26–28]. Therefore, it is a promising approach to develop spintronic devices with new functionalities by combining the current- and electric-field-induced spin-orbit coupling effects in FH system [29–31].

Here, we report an experimental study of the electric-field effect, its temperature and angular-dependence of coherent magnetization oscillation excited by current-induced SOTs in a spin current nano-oscillator based on AlO_x (15nm)/TaO_x (5 nm)/Py (3 nm)/Pt (2 nm). The coherent self-localized bullet spin-wave is excited in the central nanogap region of 3-nm thickness and 4- μ m diameter Py dish by injecting local spin current generated by bulk SHE in Pt and the IREE at both Py/Pt and Py/TaO_x interfaces. The electrostatic gating on Py/TaO_x interface through 20 nm thickness AlO_x/TaO_x insulating multilayers can shift the oscillation frequency due to gating voltage modulation of interfacial magnetic anisotropy and IREE-induced SOTs. The apparent current-dependent electric-field effects on frequencies of several spin waves at above threshold current I_{th} is caused by the combination of the nonlinearity of SCNO and the gating voltage-driven the excitation current shift, which shows a tuning rate of 4% under $V_g = \pm 5$ V, suggesting IREE provides a substantial contribution to the current-induced SOTs. Additionally, we find that these electric-field effects have an independent temperature-dependence at the studied temperature range. Electric-field modification of interfacial SOTs not only provides another ideally low-power electrical approach to locally manipulate

*Corresponding author: rhlou@nju.edu.cn

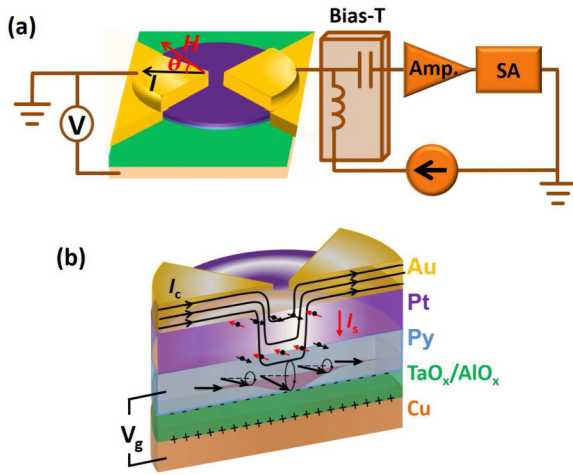


FIG. 1. (a) The schematic of the device structure and the experimental setup with the directions of current flow I and the applied magnetic field H . (b) The schematic cross-sectional view of SCNO, showing multilayer order, electrostatic gating, directions of charge-current I and spin current I_s , and spin-orbit-torque-induced oscillating magnetization region localized in the central nanogap.

spin dynamics of SCNO for spin-based information processing technologies [30–32], but also provides us some useful information and vital clue to identify the origin of SOTs in insulating oxides/ferromagnet/heavy metal trilayer structure [24].

II. EXPERIMENTAL SECTION

Figure 1(a) shows the schematic of our test device structure and the experimental setup. Our device is based on a Cu(20)/AlO_x(15)/TaO_x(5)/Py(3)/Pt(2) multilayer deposited on an annealed sapphire substrate by DC magnetron sputtering. All thicknesses are given in nanometers. The Py(3)/Pt(2) bilayer disk with 4 μ m diameter and its top two triangle-shaped Au(100 nm) electrodes with \sim 80 nm gap were electrically isolated from the 20 nm thick Cu bottom gating electrode by a 20 nm thick AlO_x(15)/TaO_x(5) bilayer [Fig. 1(b)]. The gate leakage current between the bottom Cu layer and the top Au layer is less than 0.1 nA at gate voltages of up to ± 7 V, indicating that 20 nm thick AlO_x(15)/TaO_x(5) insulating layer has a good quality. The device was fabricated by a combination of DC magnetron sputtering and electron beam lithography. The electrical current can be locally injected into the Py/Pt bilayer through two sharp triangular Au electrodes with a nanogap. In this trilayer system with broken structural inversion symmetry and both strong bulk and interfacial spin-orbit coupling, the in-plane electrical current can transfer spin torques to the Py magnetization by generating the out-of-plane spin currents flowing into the adjacent Py(3) layer due to not only the bulk SHE in Pt(2) layer, but also IREE at both Py/Pt and Py/TaO_x interfaces [24]. Similar to the previously studied nanogap SCNOs [19,33], all the measurements of microwave spectra described below are performed at in-plane magnetic field geometry with an in-plane angle θ between the in-plane field H and the direction of electrical current I , defined in Fig. 1(a).

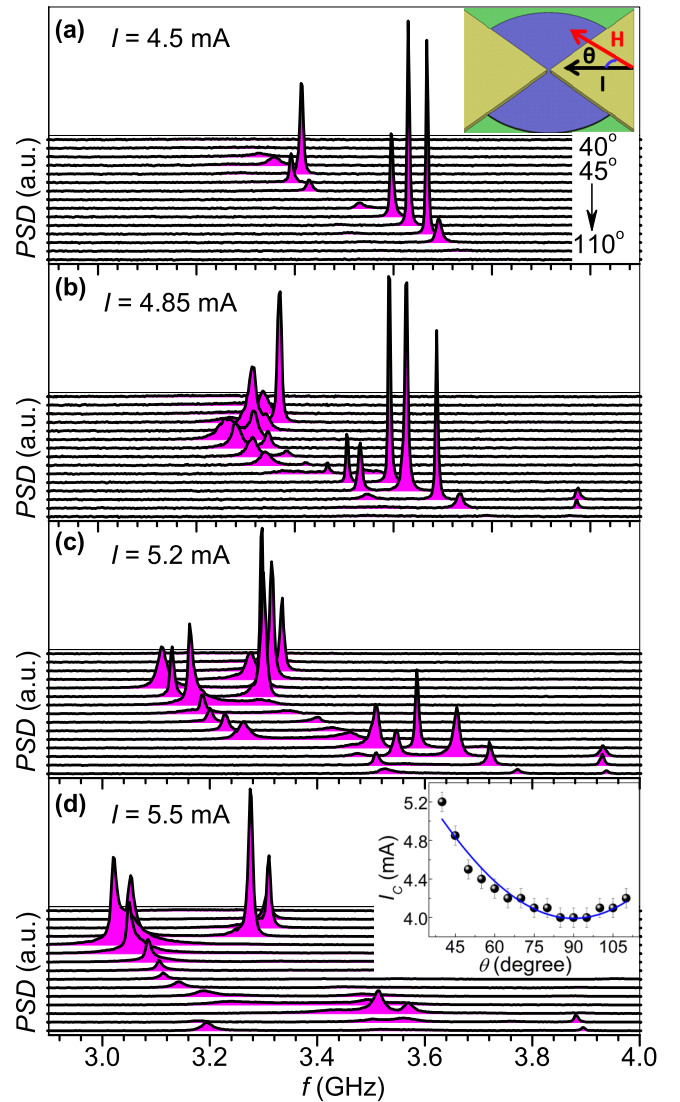


FIG. 2. Dependence of the microwave generation characteristics on the orientation of the in-plane field. Spectra obtained at θ between 40° and 110° increased in 5° steps, $H = 250$ Oe, $T = 8$ K, and $I = 4.5$ mA (a), 4.85 mA (b), 5.2 mA (c), and 5.5 mA (d). Top Inset: Schematic of the device structure and the experimental setup. Bottom Inset: Dependence of the onset current I_c on θ (circles). The solid line is the fitting curve using a cosine function.

III. RESULTS AND DISCUSSION

A. Dependence of spectral characteristics on current and the direction of magnetic field at $V_g = 0$

Measurements of the microwave generation performed at zero gate voltage $V_g = 0$ allowed us to characterize the spectral characteristics of our test devices. Figure 2 shows the dependence of the microwave generation characteristics under four representative driving currents I on θ at $V_g = 0$, $H = 250$ Oe, and $T = 8$ K. Similar to previous reported results of SCNO based on Py/Pt bilayers [18], a single microwave generation peak related to a self-localized spin wave bullet mode with frequency f below the uniform ferromagnetic resonance (FMR) frequency f_{FMR} is observed at θ between 50° and 90° at low driving current $I = 4.5$ mA [Fig. 2(a)]. There

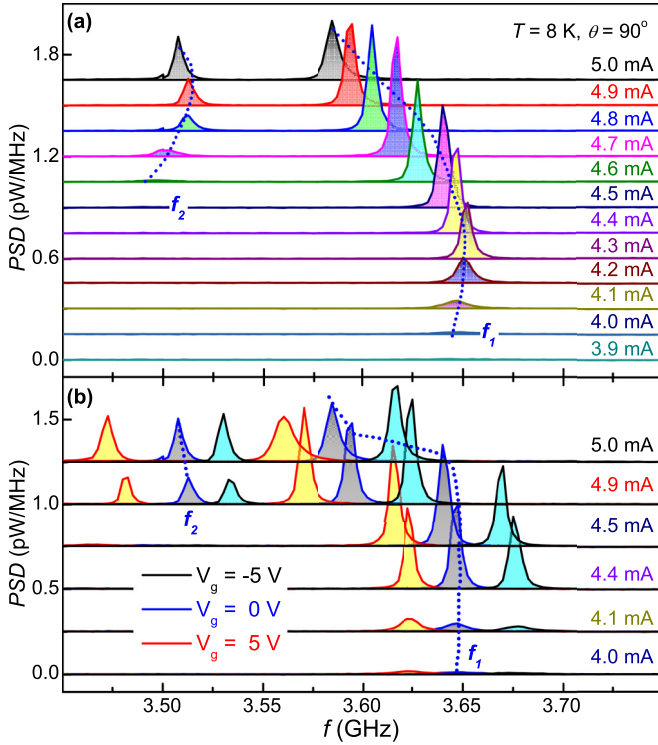


FIG. 3. (a) Dependence of the microwave generation spectra on current I from 3.9 mA to 5.0 mA increased in 0.1 mA steps, at $H = 250$ Oe, $\theta = 90^\circ$, and $T = 8$ K. Spectra has two distinct modes f_1 and f_2 at above their onset currents. (b) Same as (a) with labeled current at the gate voltage $V_g = -5$ V (black), 0 (blue), and 5 V (red). The dotted lines are given as guides to the eye.

appears an additional peak in microwave spectra when the driving current is continuously increased to above 4.85 mA [Figs. 2(b)–2(d)]. At the angles near 90° , the spectra even show three distinct peaks with the same two critical characterizations: frequency below f_{FMR} and shifting to low frequencies with increasing current (the detailed temperature and current dependence will be discussed below), indicating that all observed peaks are related to the individual spin wave bullet mode separately localized in different space regions due to the roughness of film and nano-fabrication-induced inhomogeneity. Magnetization auto-oscillation is indicated by the abrupt emergence of a sharp spectral peak at the critical current I_c . The critical current I_c versus in-plane angle θ shows a cosine functional dependence [inset of Fig. 2(d)], consistent with the out-of-plane spin current with in-plane spin polarization generated by the bulk SHE and IREE. Additionally, the value of $I_c \approx 4$ –5 mA is significantly smaller than in our previously studied thicker Py(5)/Pt(4) bilayer-based SCNOs [18,19], indicating the higher effective charge-to-spin conversion efficiency can be achieved in the relatively thin TaO_x/Py/Pt system with strong interfacial spin-orbit coupling [34,35].

B. Electric-field effect on current-driven dynamical modes

To study the electric field effect on magnetization dynamics of SCNOs, we selected two representative angles ($\theta = 60^\circ$ and 90°) to perform the microwave generation measurements

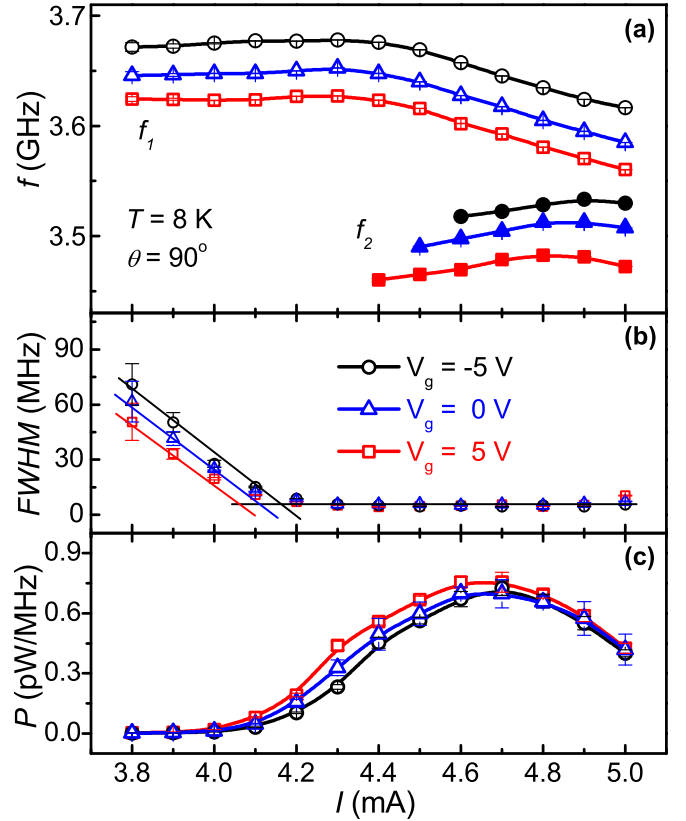


FIG. 4. Effects of electrostatic gating on the microwave generation characteristics of SCNO with the various excited current I , at $H = 250$ Oe, $\theta = 90^\circ$, and $T = 8$ K. (a)–(c) Dependence of the central generation frequency f_c of two dynamical modes (f_1 and f_2)(a), the linewidth FWHM of f_1 (b) and the intensity peak P of f_1 (c) on current I at $V_g = -5$ V (circles), 0 (triangles), and 5 V (squares). The central frequency, the linewidth, and intensity peak were determined by fitting the power spectra shown in Fig. 3 with the Lorentzian function. The solid lines in (b) are the linear fits that were used to determine the effective excitation current shift under the gating voltages, $\delta I = I(-5\text{V}) - I(5\text{V}) = 0.13 \pm 0.01$ mA.

under different gate voltages V_g . Figure 3(a) shows an example of the auto-oscillation spectra acquired without electrostatic gating at temperature $T = 8$ K, $\theta = 90^\circ$, $H = 250$ Oe, and the driving current I ranging from 3.9 to 5.0 mA. A single oscillation peak was observed first at the power spectral density (PSD) at $I = 4.0$ mA, with the central frequency of $f_1 = 3.65$ GHz significantly below the FMR frequency $f_{\text{FMR}} = 4.1$ GHz of the test device determined by the spin-torque FMR (ST-FMR) technique [35]. The frequency of the oscillation peak f_1 exhibited a small redshift with increasing current I , while its intensity increased until another peak with a lower frequency $f_2 = 3.5$ GHz appeared at $I = 4.6$ mA. Similar to mode f_1 , the lower-frequency peak also shows a redshift with increasing current in the range of high driving current. These current-dependent microwave generation characteristics indicate that the two oscillation peaks are both related to the self-localized spin-wave mode with different frequencies [18,19,36]. The coexistence of two modes with the spatial separation can be facilitated by a nano-fabrication-induced defect near the top 100-nm Au sharp-tip electrode or

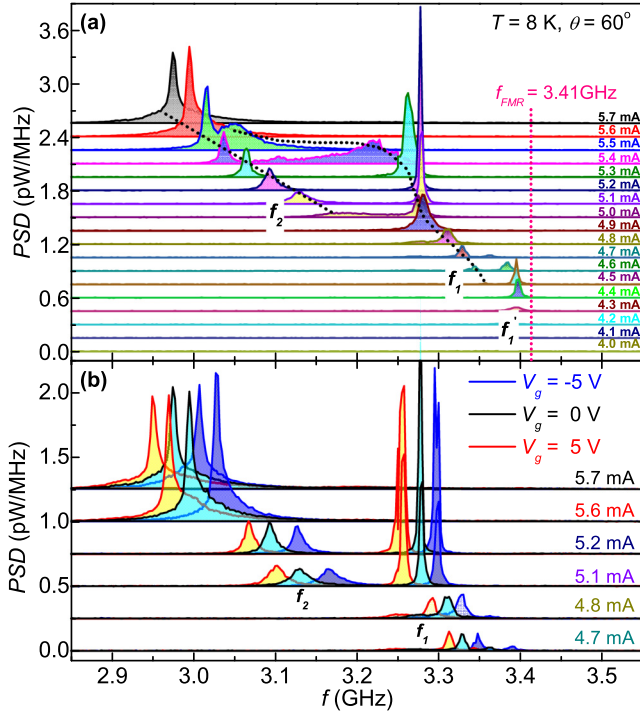


FIG. 5. (a) Dependence of the microwave generation spectra on current I from 4.0 mA to 5.7 mA increased in 0.1 mA steps, at $H = 250$ Oe, $\theta = 60^\circ$, and $T = 8$ K. Three dynamical modes with different frequencies (f_1 , f_2 , and f_{FMR}) are observed by varying current I . The FMR frequency $f_{\text{FMR}} = 3.41$ GHz (dotted line) is obtained by utilizing ST-FMR. The dotted lines are given as guides to the eye. (b) Same as (a) at the gate voltage $V_g = -5$ V (blue), 0 (black), and 5 V (red).

spatial inhomogeneity of Py(3) film. Furthermore, we analyze the dependence of the magnetization oscillation characteristics on the electric field produced by the bottom gate voltage V_g under a serial of driving currents [Fig. 3(b)]. Figure 4 shows the current dependencies of the central oscillation frequency, the full width at half maximum (FWHM), and the generation power, which are extracted from the microwave generation spectra measured at $V_g = -5, 0$, and 5 V. Figure 4(a) shows that current-dependent oscillation frequency curves under three different dc bias voltages V_g can be described as being mostly a vertical shift. Consistent with the previous studies of electric-field control of the magnetic anisotropy, the coercive field, and magnetization in thin magnetic heterostructures [7,8], our observation of electric-field-driven frequency shifts also could be attributed to the modulation of the surface magnetic anisotropy of 3-nm thick Py layers due to electric-field-driven variations of the Fermi level or even oxygen ion migration near the TaO_x/Py interface [10,25]. Furthermore, based on the gating-driven frequency shift and the Kittel formula $f = \gamma(H^2 + HH_d)^{1/2}$, we estimate that the effective demagnetizing field $H_d = 4\pi M_{\text{eff}} = 4\pi M - (2K/tM) = 8.4$ kOe has $\sim 1.1\%$ reduction under $V_g = 5$ V (or vice versa), where $\gamma = 2.8$ MHz/Oe is the gyromagnetic ratio, K and t are the anisotropy coefficient and the thickness of the Py layer.

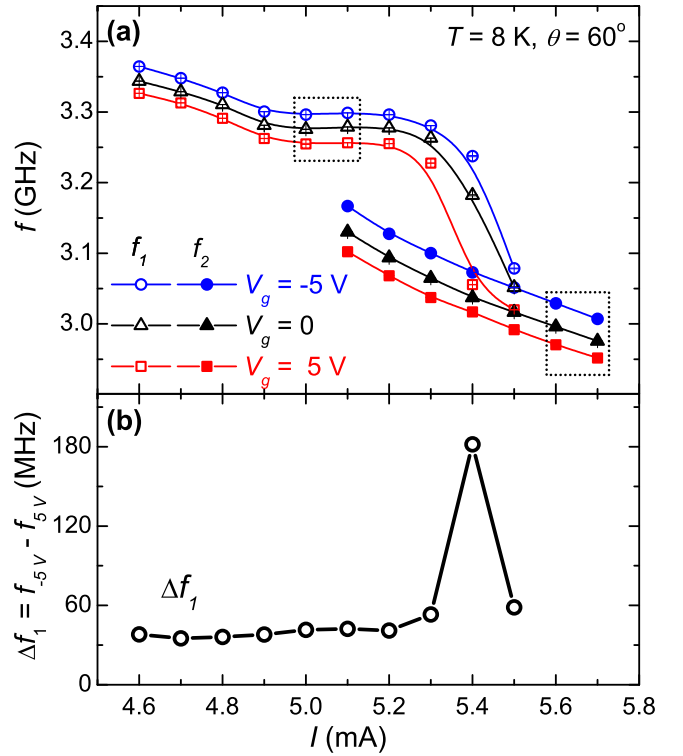


FIG. 6. Effects of electrostatic gating on the microwave generation characteristics of SCNO with the various excited currents I , at $H = 250$ Oe, $\theta = 60^\circ$, and $T = 8$ K. (a), (b) Dependence of the central generation frequency f_c of the two individual dynamical modes (f_1 and f_2) (a) and the value of voltage-driven frequency shift Δf_1 (b) of the mode f_1 on current I at $V_g = -5$ V (circles), 0 (triangles), and 5 V (squares). The central frequency was determined by fitting the power spectra shown in Fig. 5 with the Lorentzian function. The solid lines are guides to the eye. The microwave generation characteristics at certain current I represented by the dashed square outlines were selected to study the temperature dependence at the gate voltage $V_g = -5, 0$, and 5 V in Figs. 10 and 11.

At small currents, the oscillation frequency and the generation power slowly increase and the linewidth linearly decreases with increasing current, consistent with the non-linear theory of single mode of spin-torque nano-oscillation [37]. At high currents above 4.2 mA, the linewidth reaches the minimum and remains approximately constant, while the generated power rapidly increases accompanying a strong frequency redshift with increasing current. Differing from the electric-field effect on frequency discussed above, the current-dependent oscillation linewidth and generated power curves under electric fields can be approximately described as an effective shift of the driving current [Figs. 4(b) and 4(c)]. If the observed effective current shift of 65 μA at $V_g = 5$ V were caused by the modulation of H_d , the modulation rate of the effective demagnetizing field would be $dH_d/dV_g = 64$ Oe/V, as estimated from the dependence of I_c on the applied magnetic field H . This value is three times larger than estimated from the frequency shift in Fig. 4(a), indicating that anisotropy or magnetization variation alone cannot explain the observed electric-field driven current shift.

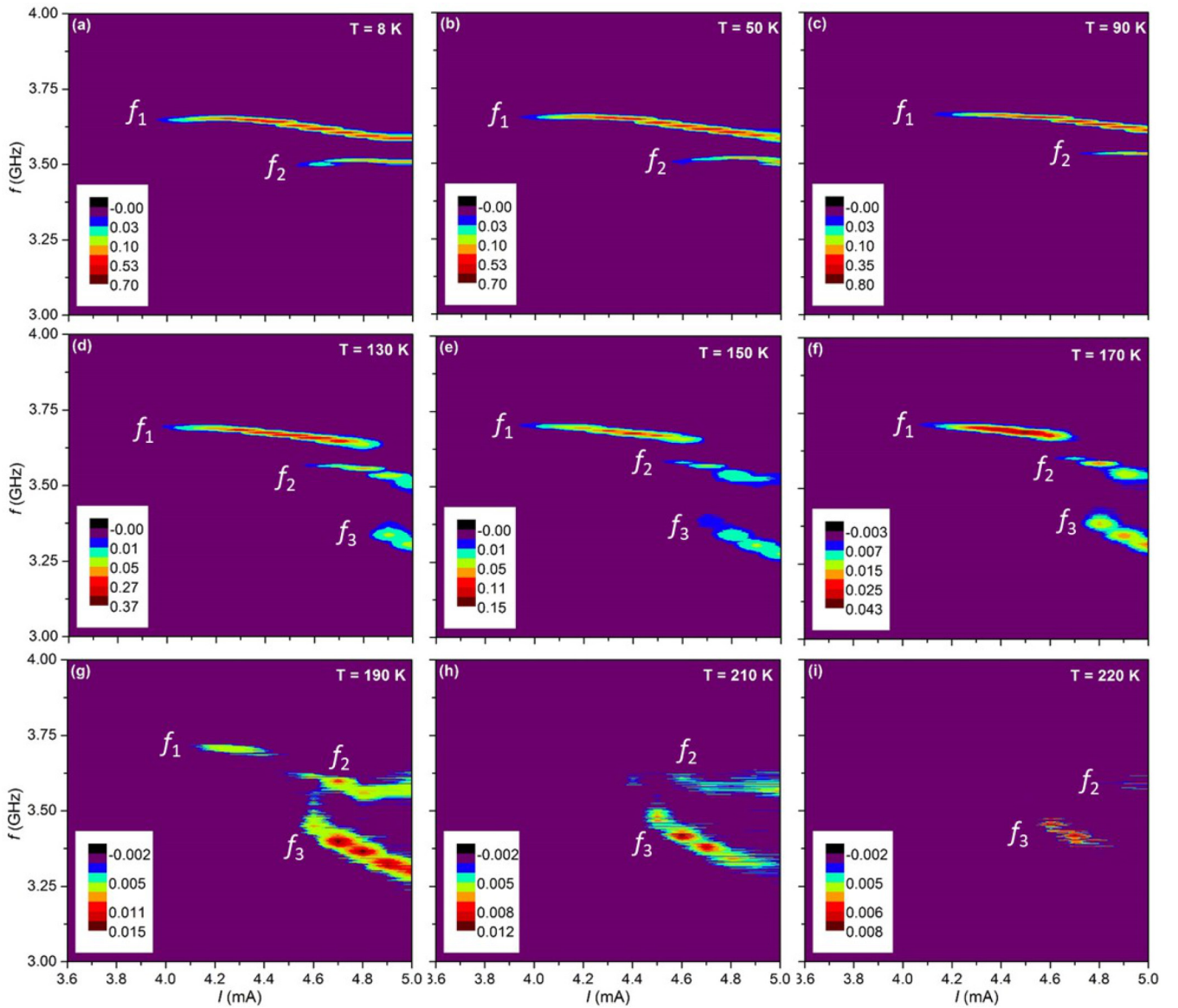


FIG. 7. Dependence of the microwave generation characteristics on current at different temperatures T , $H = 250$ Oe, and $\theta = 90^\circ$. Pseudocolor plots of the spectra obtained at above I_c increased in 0.1 mA steps, $T = 8$ K (a), 50 K (b), 90 K (c), 130 K (d), 150 K (e), 170 K (f), 190 K (g), 210 K (h), and 220 K (i).

The observed effective current shift indicates that in-plane electric current-induced SOT is modulated by gating voltage. In TaO_x/Py/Pt trilayer, except the bulk SHE in Pt(2) layer, the Py/Pt and Py/TaO_x interfaces also have a significant contribution to the SOTs due to the broken inversion symmetry and strong interfacial coupling between the electric current and the spins [22–24]. Furthermore, SOTs can be classified into dampinglike torque Γ_{\parallel} and fieldlike torque Γ_{\perp} depending on whether their directions are parallel or orthogonal to intrinsic Gilbert damping. Fieldlike torque that acts as an effective field H_{ST} can modulate the oscillation frequency while dampinglike torque counteracts Gilbert damping and directly relates to the driving current of auto-oscillation. Therefore, the voltage-dependent interfacial dampinglike torque Γ_{\parallel} is expected to result in an effective rescaling of the driving current, which can be approximately equivalent to a current shift δI . The 1.6% variation of Γ_{\parallel} at $V_g = 5$ V obtained from our mea-

surements in TaO_x/Py/Pt is slightly larger than that reported for Pt/Co/AlO_x and AlO_x/Py/Pt [26,33]. Since SCNO has a strong nonlinear frequency redshift with increasing driving current at high currents, the current shift δI due to the modulation of Γ_{\parallel} by gating voltage can also contribute to an additional frequency shift except for the modulation of H_d and H_{ST} in the nonlinear regime.

To determine whether the behaviors discussed above are the general features of SCNO, we measured and analyzed the current-dependent spectral characteristics and their electric-field effects at $\theta = 60^\circ$. Figure 5(a) shows the dependence of the microwave generation characteristics on current at $\theta = 60^\circ$, $T = 8$ K, $H = 250$ Oe, and $V_g = 0$. A high-frequency peak f_1 appears above 4.6 mA, followed by the emergence of another peak f_2 at 5.0 mA, and finally the first mode f_1 begins to transition to the regime characterized by very broad peaks and sharp frequency redshift at 5.3 mA. These behaviors are

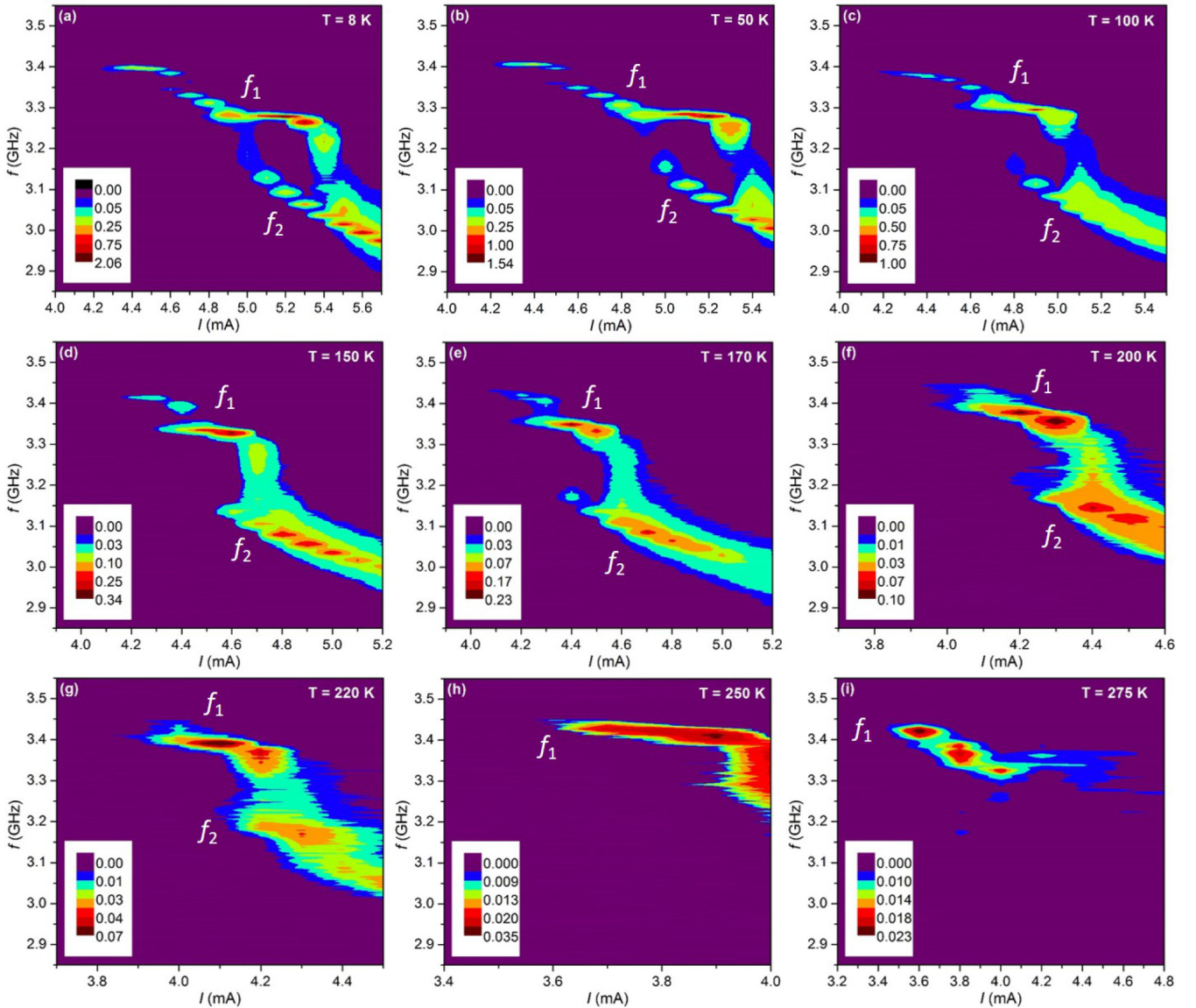


FIG. 8. Dependence of the microwave generation characteristics on current at different temperature T , $H = 250$ Oe, and $\theta = 60^\circ$. Pseudocolor plots of the spectra obtained at above I_c increased in 0.1 mA steps, $T = 8$ K (a), 50 K (b), 100 K (c), 150 K (d), 170 K (e), 200 K (f), 220 K (g), 250 K (h), and 275 K (i).

similar to those current-dependent spectral characteristics obtained at $\theta = 90^\circ$. We also observed a tiny peak f'_1 with a frequency very close to f_1 but still below $f_{\text{FMR}} = 3.41$ GHz at low currents from 4.2 mA to 4.7 mA, which may be related to a small and metastable oscillation region localized on the imperfect edge of two Au electrodes during nanofabrication process. Note that the onset of the secondary low-frequency mode f_2 does not result in the broadening of the primary high-frequency peak f_1 for both angles 60° and 90° , indicating that the two spatially separated modes are simultaneously excited and independent of each other because their spatial localization and the mode coupling due to thermal-magnon-mediated scattering are remarkably suppressed at a cryogenic temperature 8 K [38].

Figure 5(b) shows the dependence of the microwave generation characteristics of the two primary modes f_1 and f_2 on the electric field V_g . Similar to the observations at $\theta = 90^\circ$

above [Fig. 4(b)], the positive gating voltage suppresses the oscillation frequency, while the negative voltage enhances the frequency. The current dependence of the central oscillation frequency, extracted from the microwave generation spectra obtained at $V_g = -5$ V, 0, and 5 V [Fig. 5(b)], is shown in Fig. 6(a). Figure 6(b) shows that voltage-induced frequency shift Δf_1 of the mode f_1 keeps approximately a constant of 40 MHz at driving currents (≤ 5.2 , or > 5.5 mA) below or above the nonlinear crossover and is significantly enhanced by four times at the nonlinear crossover regime. These observations are well consistent with the discussed mechanisms of voltage control of the oscillation frequency above. In our studied planar SCNO, the electric-field-driven oscillation frequency shift comprises two main contributions: one from voltage control of anisotropy and magnetization, which is independent of the oscillation regime of SCNO (driving current), another from the combination of the current shift

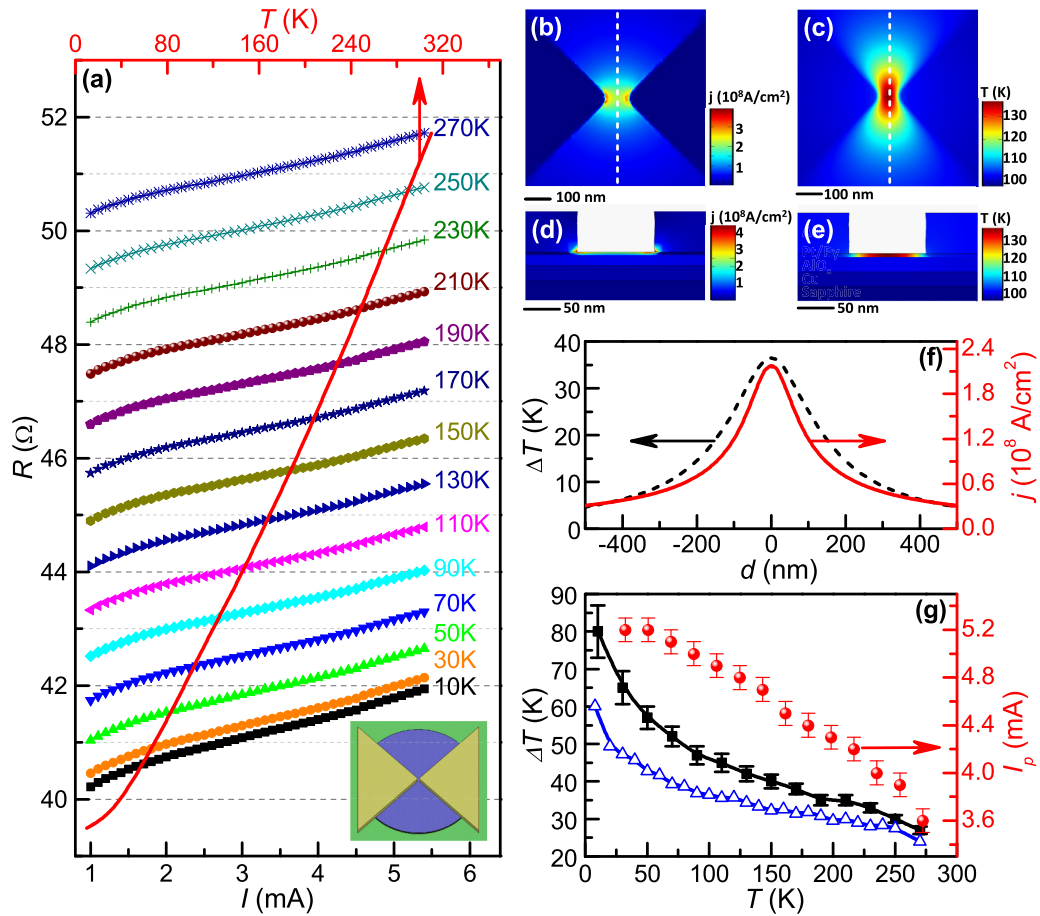


FIG. 9. Analysis of the actual device temperature T_a from resistance dependence of current and numerical calculation. (a) $R(I)$ curves at different substrate temperatures T , as labeled (bottom axis), and $R(T)$ measured with a small current (top axis). (b)–(e) Pseudocolor plots of in-plane current density j of Pt layer (b), the actual temperature T_a of Py layer (c), j (d) and T_a of the cross-section of the device at the center of electrode gap calculated by modeling the device at 4.9 mA and 100 K of substrate temperature. (f) The rising temperature $\Delta T = T_a - T$ at Py layers due to Joule heating (dotted curve, left axis) and j at Pt layer (solid curve, right axis) along the dotted lines in (c) and (b), respectively. (g) The rising temperature ΔT of the active device area at the current value I_p estimated by comparing the experimental $R(I)$ and $R(T)$ curves (squares) and numerical calculation (triangles). The dependence of I_p (right axis) corresponding to the highest peak PSD of f_1 at $\theta = 60^\circ$ on T is also shown in (g).

driven by the voltage modulation of charge-to-spin conversion efficiency and the frequency nonlinearity of SCNO. The latter highly depends on the current-dependent nonlinear regime of oscillation.

C. Temperature effect on current-driven dynamical modes

Analysis of the temperature dependence of the oscillation provides additional information to understand better the physical mechanism behind the electric-field effects and the thermal noise-induced decoherence. Figures 7 and 8 show the representative current-dependent spectra measured at different temperatures from 8 K to near room temperature, $V_g = 0$, $H = 250$ Oe, $\theta = 60^\circ$ and 90° , respectively. The spectra behaviors are qualitatively similar for all test temperatures to those observed at $T = 8$ K, which have been described and discussed in Figs. 3 and 5 above. At a representative $\theta = 90^\circ$ and $H = 250$ Oe, the current-dependent spectra exhibit clearly distinct spectral characteristics, not noticeably affected by the presence of other modes at all test tempera-

tures. For the $\theta = 60^\circ$ case, we should note that the oscillation mode f_1 has a sharp change of nonlinearity with generation power in certain current ranges accompanying a sharp frequency redshift and occur to overlap with another mode f_2 . To avoid the possible artifacts coming from the spectral overlap between the individual modes f_1 and f_2 , we focus on the temperature-dependent linewidth FWHM and voltage-driven frequency shift Δf at a current value I_p corresponding to the minimum linewidth (close to the highest peak-power density) of the mode, which is marked by the dashed squares in Fig. 6(a).

D. Joule heating effect and the actual temperature of device

To obtain the actual device temperature T_a by taking into account Joule heating, we first measured the dependence of the device resistance on current at different values of T , as illustrated by curves in Fig. 9(a). The resistance significantly increases with current, which is caused by Joule heating effects. By directly comparing $R(I)$ and $R(T)$ curves

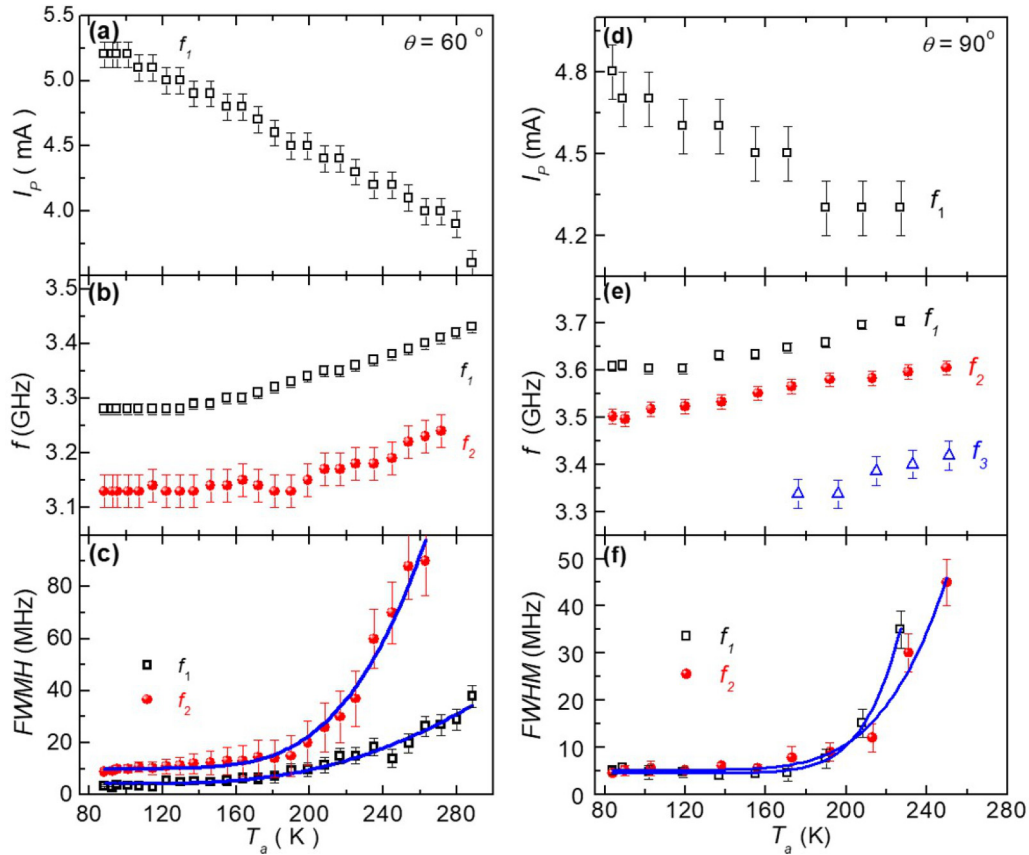


FIG. 10. Effects of temperature on the spectral characteristics of SCNO. Dependence of the current value I_p , the central generation frequency f_c and the linewidth FWHM of the dynamical modes on the actual temperature of the active device area T_a at $\theta = 60^\circ$ (a)–(c) and 90° (d)–(f). Solid lines are the results of fitting by an exponential dependence $A \exp(-E_b/k_B T) + \text{const}$ with $E_b = 96$ meV and 138 meV for f_1 and f_2 at $\theta = 60^\circ$ (c), and $E_b = 240$ meV, 170 meV for the first and second modes at $\theta = 90^\circ$ (e), respectively.

in Fig. 9(a), we can quantitatively obtain the actual device temperature T_a at a given experimental temperature T and driving current I . To further confirm the analysis from the resistance of the device and obtain the spatial distribution of the actual temperature in the Py layer, we also numerically calculate the current distribution and Joule heating with the COMSOL MULTIPHYSICS package using the previously reported resistivity and thermal conductivity of Py/Pt thin films, Au and sapphire substrate, and their interface thermal resistance [39–44]. As expected, the current is strongly localized in the nanogap region with the maximum under the end of Au tips [Figs. 9(b), 9(d), and 9(f)]. Figure 9(c) shows that the temperature of the Py layer is locally increased in the center region of the device. At a representative driving current of 4.9 mA and substrate temperature of 100 K, the cross section of the rising temperature distribution due to Joule heating through the center of the device along the direction perpendicular to the current flow exhibits a maximum of about 35 K at the center of nanogap [Fig. 9(f)]. Figure 9(g) shows the Joule heating-induced rising temperature of the active device area at the current value I_p estimated by comparing the experimental $R(I)$ and $R(T)$ curves and numerical calculation, respectively. The calculation and experimental results ΔT show similar temperature-dependent behavior but the value estimated from $R(T)$ of the device is small than that of numerical calculation.

One possible reason for the difference is that ΔT obtained from the resistance data is the mean value, rather than the peak value of the numerical calculation [Fig. 9(f)].

E. Temperature dependence of spectral linewidth and electric-field effect

Figure 10(a) shows that I_p of the dynamical mode f_1 decreases from 5.2 mA at $T_a = 88$ K to 3.6 mA at $T_a = 288$ K. The similar temperature dependence for the excited dynamical modes at $\theta = 90^\circ$ are also observed in Fig. 10(d). The increase of the excitation efficiency with increasing temperatures may be caused by a decrease of the Py magnetization \mathbf{M} , an increase of SHE- and/or IREE-induced SOT efficiency, or a decrease of the dynamical damping of the thin Py layer. Temperature-dependent ST-FMR and static magnetization measurements indicate that \mathbf{M} does not significantly decrease with increasing T over the studied temperature range. Meanwhile, the oscillation frequencies of all observed self-localized spin-wave modes show an unexpected weak increase with increasing T [Figs. 10(b) and 10(e)]. Therefore, the weak temperature-dependent \mathbf{M} is not the reason that the value of driving current I_p obviously decreases with increasing T . The observed behaviors are likely associated with the increase of SOT efficiency or decreased damping of oscillation with

increasing T . The previously reported temperature-dependent Gilbert damping in Py thin films found that Gilbert damping of Py films with thickness < 5 nm shows a significant enhancement with a broad peak at ~ 50 K, distinctly differing from a monotonic decrease with decreasing T observed in the thick Py film. The increase of oscillation frequency with increasing T may be related to the enhanced nonlinear interaction between thermally excited linear mode with a high frequency and SOT-driven localized bullet mode with a low frequency due to increasing thermal magnon scattering at high temperature, warranting further theoretical studies of the temperature dependence of this effect. In addition, the temperature dependence of the generation linewidth of spin-wave modes also provides important information about thermal effects on the magnetization dynamics, such as decoherence and mechanism of mode coupling. Previous theoretical and experimental studies showed that the nonlinearity could dramatically reduce the oscillation coherence due to the fluctuations of oscillation amplitude-induced the phase noise [45–47]. To avoid the anomalous contributions due to current-dependent variations of nonlinearity, as the oscillation frequency discussed in Figs. 10(b) and 10(e) above, we analyze the temperature-dependent linewidth behaviors at current corresponding to the minimum value of the linewidth, where such anomalous effects are expected to be small. Figures 10(c) and 10(f) show that the minimum linewidth of the dynamical modes remain approximately constant at $T_a < 180$ K, and then exponentially increase at larger T_a . This dependence is similar to the previous observation in SCNO with thick Py(5)/Pt(4) bilayer [19], but qualitatively different from the linear dependence observed in a single-mode auto-oscillator, such as nanocontact spin-transfer nano-oscillator [48,49], magnetic vortex oscillators [50], and SCNO with perpendicular magnetic anisotropy [51]. These linewidth increasing exponentially with temperature should be related to the thermally activated transitions between different dynamical modes (f_1 , f_2 , and f_3) [47,48]. Furthermore, we use the two-state fluctuation model to fit the four temperature-dependent FWHM curves with $A \exp(-E_b/k_B T) + \text{const}$, where E_b is the energy barrier between the two states and k_B is the Boltzmann constant. The fitting values of E_b are 100 meV and 130 meV for the modes f_1 and f_2 , respectively, at $\theta = 60^\circ$, almost half of the values of 240 meV and 170 meV at $\theta = 90^\circ$, indicating that the modes excited at 60° are more easy to be thermally activated than at 90° . These fitting results are consistent with that the oscillation frequencies of three individual modes are strictly separated at 90° (Fig. 7), while the spatially separated two modes (f_1 and f_2) have some overlapping frequency region at larger current for 60° .

As discussed above, the electric-field can shift the oscillation frequencies of dynamical modes by voltage modulation of magnetization or magnetic anisotropy, magnetic damping, and current-induced SOTs. We now further analyze the temperature dependence of these electric-field effects on oscillation frequency shift. Figure 11 shows temperature dependence of electric-field-induced central generation frequency shift Δf of the dynamical modes at I_p , marked by the dashed square in Fig. 6, at $\theta = 60^\circ$ and 90° . Voltage-induced frequency shifts of all five modes show a temperature-independent behavior for the studied temperature range from

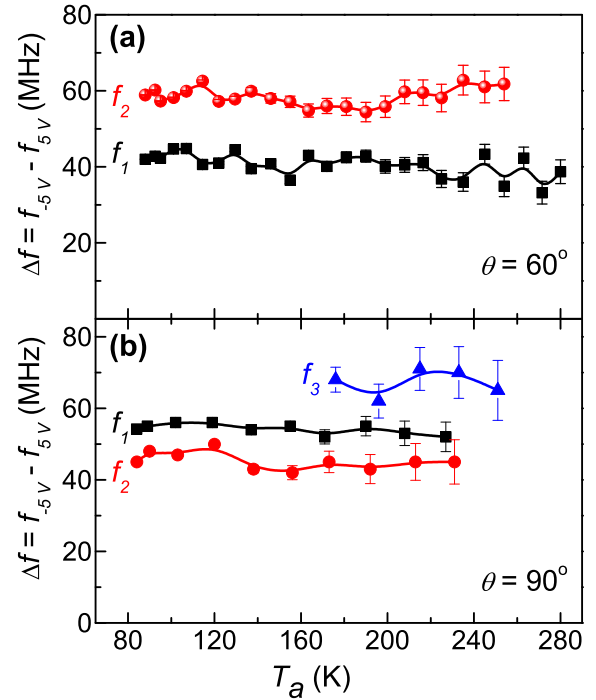


FIG. 11. Temperature dependence of electric-field-induced central generation frequency shift Δf of three dynamical modes. $\Delta f = f_{-5V} - f_{5V}$ vs T_a at I_p , $\theta = 60^\circ$ (a) and $\theta = 90^\circ$ (b). The solid curves are given as guides to the eye.

$T_a = 80$ K to 280 K. At $\theta = 60^\circ$, the value of Δf of f_1 is above 4 MHz/V, significantly smaller than 6 MHz/V of f_2 . The reason for the difference of frequency shift is that f_2 has a higher nonlinearity factor than f_1 at their driving currents I_p (Fig. 8) because of the combination of nonlinearity and voltage-driven driving current shift as one of two dominated contribution to the frequency shift, which has been detailedly discussed in Figs. 4 and 6 above. Note that the voltage modulation of magnetization or magnetic anisotropy should cause an appropriately same frequency shift for all modes with very close-by oscillation frequencies. Similar to the $\theta = 60^\circ$ case, the current-dependent spectra in Fig. 7 show that f_1 has a higher nonlinearity factor than f_2 , but lower than f_3 . Therefore, for 90° , it is expect to have the minimum Δf value of 4.5 MHz/V for f_2 , the middle value of 5.5 MHz/V for f_1 , and the maximum value of 7 MHz/V for f_3 , respectively.

IV. CONCLUSION

In summary, we demonstrate that magnetization dynamical states, excited by SOTs generated from the bulk SHE and interfacial Rashba-Edelstein effect in a spin torque nano-oscillator based on TaO_x/Py(3)/Pt(2) trilayers, can be controlled by driving current and electrostatic gating. The former control of the frequency of this self-localized bullet mode is dominated by the nonlinearity of spin-torque oscillators, while the latter has two main contributions: one is gating voltage modulation of the interfacial magnetic anisotropy,

another one is the driving current shift due to gating voltage modulation of IREE. The decoherence of the localized modes is dominated by thermally activated mode transition evidenced by an exponential linewidth broadening with increasing temperature at higher temperatures, which is significantly suppressed at cryogenic temperatures $T_a < 160$ K. The electrostatic gating-induced oscillation frequency shift gets enhanced in the strongly nonlinear oscillation regime but exhibits a temperature-independent behavior. Our results not only provide insight into the mechanisms about current-induced SOTs in the typical ferromagnetic trilayers but also provide an efficient method to electrically

control spin dynamics for the development of magnon-based electronics.

ACKNOWLEDGMENTS

This work was supported by the National Natural Science Foundation of China (Grants No. 11774150, No. 12074178, and No. 12004171), the National Key Research and Development Program of China (Grant No. 2016YFA0300803), the Natural Science Foundation of Jiangsu Province (Grant No. BK20200309), and the Open Research Fund of Jiangsu Provincial Key Laboratory for Nanotechnology.

-
- [1] F. Matsukura, Y. Tokura, and H. Ohno, *Nat. Nanotechnol.* **10**, 209 (2015).
- [2] C. Song, B. Cui, F. Li, X. J. Zhou, and F. Pan, *Prog. Mater. Sci.* **87**, 33 (2017).
- [3] A. Brataas, A. D. Kent, and H. Ohno, *Nat. Mater.* **11**, 372 (2012).
- [4] A. Manchon, J. Zelezny, I. M. Miron, T. Jungwirth, J. Sinova, A. Thiaville, K. Garello, and P. Gambardella, *Rev. Mod. Phys.* **91**, 035004 (2019).
- [5] V. Garcia, M. Bibes, L. Bocher, S. Valencia, F. Kronast, A. Crassous, X. Moya, S. Enouz-Vedrenne, A. Gloter, D. Imhoff, C. Deranlot, N. D. Mathur, S. Fusil, K. Bouzehouane, and A. Barthelémy, *Science* **327**, 1106 (2010).
- [6] J. T. Heron, M. Trassin, K. Ashraf, M. Gajek, Q. He, S. Y. Yang, D. E. Nikonov, Y. H. Chu, S. Salahuddin, and R. Ramesh, *Phys. Rev. Lett.* **107**, 217202 (2011).
- [7] M. Weisheit, S. Faehler, A. Marty, Y. Souche, C. Poinsgnon, and D. Givord, *Science* **315**, 349 (2007).
- [8] T. Maruyama, Y. Shiota, T. Nozaki, K. Ohta, N. Toda, M. Mizuguchi, A. A. Tulapurkar, T. Shinjo, M. Shiraishi, S. Mizukami, Y. Ando, and Y. Suzuki, *Nat. Nanotechnol.* **4**, 158 (2009).
- [9] Y. Shiota, T. Nozaki, F. Bonell, S. Murakami, T. Shinjo, and Y. Suzuki, *Nat. Mater.* **11**, 39 (2012).
- [10] C. Bi, Y. Liu, T. Newhouse-Illige, M. Xu, M. Rosales, J. W. Freeland, O. Mryasov, S. Zhang, S. G. E. te Velthuis, and W. G. Wang, *Phys. Rev. Lett.* **113**, 267202 (2014).
- [11] J. C. Slonczewski, *J. Magn. Magn. Mater.* **159**, L1 (1996); **195**, L261 (1999).
- [12] L. Berger, *Phys. Rev. B.* **54**, 9353 (1996); *J. Appl. Phys.* **90**, 4632 (2001).
- [13] M. Tsoi, A. G. M. Jansen, J. Bass, W. C. Chiang, M. Seck, V. Tsoi, and P. Wyder, *Phys. Rev. Lett.* **80**, 4281 (1998); **81**, 493(E) (1998).
- [14] J. A. Katine, F. J. Albert, R. A. Buhrman, E. B. Myers, and D. C. Ralph, *Phys. Rev. Lett.* **84**, 3149 (2000).
- [15] I. M. Miron, G. Gaudin, S. Auffret, B. Rodmacq, A. Schuhl, S. Pizzini, J. Vogel, and P. Gambardella, *Nat. Mater.* **9**, 230 (2010).
- [16] T. Suzuki, S. Fukami, N. Ishiwata, M. Yamanouchi, S. Ikeda, and N. Kasai, and H. Ohno, *Appl. Phys. Lett.* **98**, 142505 (2011).
- [17] L. Q. Liu, C. F. Pai, Y. Li, H. W. Tseng, D. C. Ralph, and R. A. Buhrman, *Science* **336**, 555 (2012).
- [18] V. E. Demidov, S. Urazhdin, H. Ulrichs, V. Tiberkevich, A. Slavin, D. Baither, G. Schmitz, and S. O. Demokritov, *Nat. Mater.* **11**, 1028 (2012).
- [19] R. H. Liu, W. L. Lim, and S. Urazhdin, *Phys. Rev. Lett.* **110**, 147601 (2013).
- [20] M. I. D'yakonov and V. I. Perel, *JETP Lett.* **13**, 467 (1971).
- [21] J. E. Hirsch, *Phys. Rev. Lett.* **83**, 1834 (1999).
- [22] Y. A. Bychkov and E. I. Rashba, *J. Phys. C* **17**, 6039 (1984); G. Dresselhaus, *Phys. Rev.* **100**, 580 (1955).
- [23] A. Manchon and S. Zhang, *Phys. Rev. B* **79**, 094422 (2009).
- [24] V. P. Amin, P. M. Haney, and M. D. Stiles, *J. Appl. Phys.* **128**, 151101 (2020).
- [25] L. Xu and S. F. Zhang, *J. Appl. Phys.* **111**, 07C501 (2012).
- [26] R. H. Liu, W. L. Lim, and S. Urazhdin, *Phys. Rev. B* **89**, 220409(R) (2014).
- [27] K. M. Cai, M. Y. Yang, H. L. Ju, S. M. Wang, Y. Ji, B. H. Li, K. W. Edmonds, Y. Sheng, B. Zhang, N. Zhang, S. Liu, H. Z. Zheng, and K. Y. Wang, *Nat. Mater.* **16**, 712 (2017).
- [28] H. Fulara, M. Zahedinejad, R. Khymyn, M. Dvornik, S. Fukami, S. Kanai, H. Ohno, and J. Akerman, *Nat. Commun.* **11**, 4006 (2020).
- [29] B. Rana and Y. Otani, *Commun. Phys.* **2**, 90 (2019).
- [30] J. P. Xu, L. C. Jin, Z. M. Liao, Q. Wang, X. L. Tang, Z. Y. Zhong, and H. W. Zhang, *Front. Mater.* **7**, 25 (2020).
- [31] V. E. Demidov, S. Urazhdin, A. Anane, V. Cros, and S. O. Demokritov, *J. Appl. Phys.* **127**, 170901 (2020).
- [32] L. Li, L. Chen, R. H. Liu, and Y. W. Du, *Chin. Phys. B* **29**, 117102 (2020).
- [33] R. H. Liu, L. Chen, S. Urazhdin, and Y. W. Du, *Phys. Rev. Appl.* **8**, 021001(R) (2017).
- [34] Minh-Hai Nguyen, D. C. Ralph, and R. A. Buhrman, *Phys. Rev. Lett.* **116**, 126601 (2016).
- [35] L. Yang, Y. Fei, K. Zhou, L. Chen, Q. Fu, L. Li, C. Yan, H. Li, Y. W. Du, and R. H. Liu, *Appl. Phys. Lett.* **118**, 032405 (2021).
- [36] A. Slavin and V. Tiberkevich, *Phys. Rev. Lett.* **95**, 237201 (2005).
- [37] A. Slavin and V. Tiberkevich, *IEEE Trans. Magn.* **45**, 1875 (2009).
- [38] L. Chen, S. Urazhdin, Y. W. Du, and R. H. Liu, *Phys. Rev. Appl.* **11**, 064038 (2019).
- [39] COMSOL Multiphysics, COMSOL AB, Stockholm, Sweden. www.comsol.com.

- [40] E. T. Swartz and R. O. Pohl, *Appl. Phys. Lett.* **51**, 2200 (1987).
- [41] H. K. Lyeo and D. G. Cahill, *Phys. Rev. B* **73**, 144301 (2006).
- [42] R. J. Stoner and H. J. Maris, *Phys. Rev. B* **48**, 16373 (1993).
- [43] X. Zhang, Q. G. Zhang, B. Y. Cao, M. Fujin, K. Takahashi, and T. Ikuta, *Chin. Phys. Lett.* **23**, 936 (2006).
- [44] E. Ramos, C. Lopez, J. Akerman, M. Munoz, and J. L. Prieto, *Phys. Rev. B* **91**, 214404 (2015).
- [45] V. S. Tiberkevich, A. N. Slavin, and J. V. Kim, *Phys. Rev. B* **78**, 092401 (2008).
- [46] T. J. Silva and M. W. Keller, *IEEE Trans. Magn.* **46**, 3555 (2010).
- [47] P. K. Muduli, O. G. Heinonen, and J. Åkerman, *Phys. Rev. B* **86**, 174408 (2012).
- [48] M. L. Schneider, W. H. Rippard, M. R. Pufall, T. Cecil, T. J. Silva, and S. E. Russek, *Phys. Rev. B* **80**, 144412 (2009).
- [49] J. F. Sierra, M. Quinsat, F. Garcia-Sanchez, U. Ebels, I. Joumard, A. S. Jenkins, B. Dieny, M. C. Cyrille, A. Zeltser, and J. A. Katine, *Appl. Phys. Lett.* **101**, 062407 (2012).
- [50] P. Bortolotti, A. Dussaux, J. Grollier, V. Cros, A. Fukushima, H. Kubota, K. Yakushiji, S. Yuasa, K. Ando, and A. Fert, *Appl. Phys. Lett.* **100**, 042408 (2012).
- [51] L. Chen, S. Urazhdin, K. Zhou, Y. W. Du, and R. H. Liu, *Phys. Rev. Appl.* **13**, 024034 (2020).